93-GT-94

THE AMERICAN SOCIETY OF MECHANICAL ENGINEERS
345 E. 47th St., New York, N.Y. 10017

A LINEARIZED EULER ANALYSIS OF UNSTEADY TRANSONIC FLOWS IN TURBOMACHINERY

Kenneth C. Hall, William S. Clark, and Christopher B. Lorence
Department of Mechanical Engineering and Materials Science
Duke University
Durham, North Carolina

ABSTRACT

A computational method for efficiently predicting unsteady transonic flows in two- and three-dimensional cascades is presented. The unsteady flow is modelled using a linearized Euler analysis whereby the unsteady flow field is decomposed into a nonlinear mean flow plus a linear harmonically varying unsteady flow. The equations that govern the perturbation flow, the linearized Euler equations, are linear variable coefficient equations. For transonic flows containing shocks, shock capturing is used to model the shock impulse (the unsteady load due to the harmonic motion of the shock). A conservative Lax-Wendroff scheme is used to obtain a set of linearized finite volume equations that describe the harmonic small disturbance behavior of the flow. Conditions under which such a discretization will correctly predict the shock impulse are investigated. Computational results are presented that demonstrate the accuracy and efficiency of the present method as well as the essential role of unsteady shock impulse loads on the flutter stability of fans.

NOMENCLATURE

A	=	channel height
B	=	model equation source term coefficient
$\mathbf{b}$	=	inhomogenous part of linearized Euler equations
C_m	=	unsteady pitching moment coefficient
$C_p,\ c_p$	=	mean and unsteady coefficient of pressure $(P - P_{-\infty})/(\rho V^2/2)$
$\hat{e}$	=	internal energy
$f,\ g,\ h$	=	grid motion perturbation functions
$\hat{\mathbf{F}},\ \hat{\mathbf{G}},\ \hat{\mathbf{H}}$	=	Euler equations flux vectors
$\mathbf{F},\ \mathbf{G},\ \mathbf{H}$	=	Euler equations mean flow flux vectors
$\hat{F}$	=	model equation flux
F	=	model equation mean flow flux
G	=	linear blade-to-blade gap
$g(x,t)$	=	test function
$\hat{I}$	=	rothalpy
I	=	impulse
j	=	$\sqrt{-1}$
M	=	Mach number
$\hat{P}$	=	model equation "pressure"
P	=	model equation mean flow "pressure"
$\hat{p}$	=	static pressure
r	=	distance from x-axis
R	=	over-relaxation factor
$\hat{\mathbf{S}}$	=	Euler equation source term
$\mathbf{S}$	=	Euler equation mean flow source term
t	=	time
$\hat{u},\ \hat{v},\ \hat{w}$	=	Cartesian components of velocity
$\hat{\mathbf{U}}$	=	vector of conservation variables
$\mathbf{U},\ \mathbf{u}$	=	mean, perturbation conservation variables
$\hat{U}$	=	model equation conservation variable
$U,\ u$	=	model equation mean and perturbation conservation variable
X_s	=	mean shock location
x_s	=	complex amplitude of shock motion
$x,\ y,\ z$	=	Cartesian coordinates
β	=	inflow angle measured from axial direction
γ	=	ratio of specific heats
Θ	=	stagger angle
$\xi,\ \eta,\ \zeta$	=	computational coordinates
$\hat{\rho}$	=	static density
σ	=	interblade phase angle
τ	=	time in computational coordinates
$\omega,\ \overline{\omega}$	=	dimensional and reduced frequencies
Ω	=	shaft rotation rate

Subscripts

i	=	grid index
p	=	due to perturbation in pressure
T	=	total or stagnation quantity
u	=	due to perturbation in conservation variable
$-\infty,\ \infty$	=	far upstream and downstream regions

Superscripts

n	=	time index

Presented at the International Gas Turbine and Aeroengine Congress and Exposition
Cincinnati, Ohio May 24–27, 1993
This paper has been accepted for publication in the Transactions of the ASME
Discussion of it will be accepted at ASME Headquarters until September 30,1993

INTRODUCTION

In recent years, a number of linearized flow analyses have been developed to compute unsteady flows in cascades, especially the unsteady flows that produce the aeroelastic phenomena of flutter and forced response. The unsteady aerodynamic loads acting on transonic airfoils in cascades are composed of two parts: the unsteady pressure distribution away from the shock, and a "shock impulse" load that acts where the shock impinges on the airfoil surface. This shock impulse arises from the unsteady motion of the shock. Accurate prediction of the shock impulse is important since the unsteady aerodynamic load due to the shock impulse is of the same order as the unsteady aerodynamic loads due to the unsteady pressure away from the shock. In viscous flows, the shock is smeared near the airfoil surface due to shock/boundary layer interaction and hence, strictly speaking, no shock impulse exists at the surface. Away from the airfoil, however, the shock wave is very thin, typically on the order of a few mean free paths thick, and the concept of a shock impulse is important in connecting the regions of smooth flow on either side of the shock.

Verdon et al (Verdon and Caspar, 1984; Verdon, 1987) and Whitehead (1987, 1990) have developed linearized potential analyses of two-dimensional subsonic and transonic flows in cascades. Both Verdon and Whitehead have used shock capturing to model unsteady shock loads. Verdon has also used shock fitting in his linearized potential analysis to explicitly model the shock motion. Because of the assumption of isentropic and irrotational flow, however, these potential analyses cannot be used to model unsteady flows with strong shocks, flows with shocks that span the blade passage, or general three-dimensional flows. For this reason, investigators have begun to develop linearized Euler analyses of unsteady cascade flows (Hall and Crawley, 1989; Hall and Clark, 1991a; Holmes and Chuang, 1991; Kahl and Klose, 1991; Hall and Lorence, 1992). Hall and Crawley (1989) have shown that shock fitting can be implemented within the framework of a linearized Euler analysis to model accurately the unsteady motion of shocks. However, due to the inherent complexity of shock fitting algorithms, one would prefer to use the simpler shock capturing technique to model the shock impulse.

While shock capturing is favored for its simplicity, it has only recently been shown that the shock impulse load can be modelled properly using shock capturing within a linearized framework. There are two approaches that have been suggested for obtaining discretizations of the linearized Euler equations. The first approach, referred to in this paper as Method I, is to first discretize the nonlinear unsteady Euler equations and then linearize the resulting finite difference equations. The second approach, Method II, is to first linearize the nonlinear unsteady Euler equations, then discretize the resulting linearized equations using traditional finite difference or finite volume techniques. Lindquist (1991) and Lindquist and Giles (1991a and 1991b) have argued that the unsteady shock loads will be correctly predicted provided the linearized code is a Method I type linearization of a time-accurate, conservative, nonlinear flow solver. Their results thus far, however, have been limited to quasi-one-dimensional channel flows. Furthermore, they do not discuss the conditions under which Method II linearizations will properly model the shock impulse.

The objectives of this paper are twofold. First, we demonstrate mathematically and by numerical experiment that the requirement put forth by Lindquist and Giles that the linearization be a Method I linearization of an unsteady nonlinear scheme is too stringent. We show that Method II linearizations will also work as long as the finite difference representation of the linearized Euler equations is conservative. Second, having demonstrated that conservative Method II linearizations may be used to properly model the unsteady shock impulse, we present a linearized Euler analysis (Method II type) of unsteady two- and three-dimensional flow in cascades. Ni's Lax-Wendroff scheme (Ni, 1982) is used to obtain a finite volume representation of the unsteady linearized Euler equations. Computational results are presented for both two- and three-dimensional unsteady transonic flows in cascades. Some of these calculations are compared to those computed using a nonlinear time-marching shock capturing Euler analysis. It is shown that the present unsteady linearized analysis agrees quite well with the nonlinear analysis. The computed results also demonstrate that the unsteady shock loads can provide a destabilizing influence on the flutter stability of cascades.

Theory

Flow Field Description

In this paper, we assume that the unsteady flow is inviscid and adiabatic, and that the unsteady flow in a cascade may be modelled by the Euler equations. For a three-dimensional rotating Cartesian coordinate system, the Euler equations are given by

$$\frac{\partial \hat{\mathbf{U}}}{\partial t} + \frac{\partial \hat{\mathbf{F}}}{\partial x} + \frac{\partial \hat{\mathbf{G}}}{\partial y} + \frac{\partial \hat{\mathbf{H}}}{\partial z} - \hat{\mathbf{S}} = 0 \qquad (1)$$

where $\hat{\mathbf{U}}$ is the vector of conservation variables, $\hat{\mathbf{F}}$, $\hat{\mathbf{G}}$, and $\hat{\mathbf{H}}$ are the so-called flux vectors, and $\hat{\mathbf{S}}$ is a vector of source terms arising from centrifugal and Coriolis forces. These vector quantities are given by

$$\hat{\mathbf{U}} = \begin{bmatrix} \hat{\rho} \\ \hat{\rho}\hat{u} \\ \hat{\rho}\hat{v} \\ \hat{\rho}\hat{w} \\ \hat{e} \end{bmatrix}, \quad \hat{\mathbf{F}} = \begin{bmatrix} \hat{\rho}\hat{u} \\ \hat{\rho}\hat{u}^2 + \hat{p} \\ \hat{\rho}\hat{u}\hat{v} \\ \hat{\rho}\hat{u}\hat{w} \\ \hat{\rho}\hat{u}\hat{I} \end{bmatrix}, \quad \hat{\mathbf{G}} = \begin{bmatrix} \hat{\rho}\hat{v} \\ \hat{\rho}\hat{u}\hat{v} \\ \hat{\rho}\hat{v}^2 + \hat{p} \\ \hat{\rho}\hat{v}\hat{w} \\ \hat{\rho}\hat{v}\hat{I} \end{bmatrix},$$

$$\hat{\mathbf{H}} = \begin{bmatrix} \hat{\rho}\hat{w} \\ \hat{\rho}\hat{u}\hat{w} \\ \hat{\rho}\hat{v}\hat{w} \\ \hat{\rho}\hat{w}^2 + \hat{p} \\ \hat{\rho}\hat{w}\hat{I} \end{bmatrix}, \quad \hat{\mathbf{S}} = \begin{bmatrix} 0 \\ 0 \\ \hat{\rho}\left(\Omega^2 y - 2\Omega\hat{w}\right) \\ \hat{\rho}\left(\Omega^2 z + 2\Omega\hat{v}\right) \\ 0 \end{bmatrix}$$

where $\hat{\rho}$ is the density, $\hat{p}$ is the pressure, $\hat{u}$, $\hat{v}$, and $\hat{w}$ are the x, y, and z components of velocity, $\hat{e}$ is the internal energy, and $\hat{I}$ is the rothalpy. Here we have assumed that the coordinate system is rotating about the x-axis with rotational speed Ω. The pressure, $\hat{p}$, and the rothalpy, $\hat{I}$, are given by

$$\hat{p} = (\gamma - 1)\left[\hat{e} - \frac{1}{2}\hat{\rho}\left(\hat{u}^2 + \hat{v}^2 + \hat{w}^2\right) + \frac{1}{2}\hat{\rho}\Omega^2 r^2\right]$$

and

$$\hat{I} = \frac{\hat{e} + \hat{p}}{\hat{\rho}} = \frac{\gamma}{\gamma - 1}\frac{\hat{p}}{\hat{\rho}} + \frac{1}{2}\left(\hat{u}^2 + \hat{v}^2 + \hat{w}^2\right) - \frac{1}{2}\Omega^2 r^2$$

Where r is the distance from the x-axis ($r = \sqrt{y^2 + z^2}$).

Next, we would like to determine the small disturbance behavior of Eq. (1) due to, for example, the fluttering motion of

the blades of the cascade. To improve the accuracy of these calculations, a number of investigators have proposed the use of a harmonically deforming computational grid (Huff, 1989; Hall and Clark, 1991a and 1991b; Holmes and Chuang, 1991; Hall and Lorence, 1992). The motion of the grid is defined by

$$x(\xi,\eta,\zeta,\tau) = \xi + f(\xi,\eta,\zeta)e^{j\omega t} \quad (2a)$$
$$y(\xi,\eta,\zeta,\tau) = \eta + g(\xi,\eta,\zeta)e^{j\omega t} \quad (2b)$$
$$z(\xi,\eta,\zeta,\tau) = \zeta + h(\xi,\eta,\zeta)e^{j\omega t} \quad (2c)$$
$$t(\xi,\eta,\zeta,\tau) = \tau \quad (2d)$$

where ω is the frequency of vibration of the blades, and where f, g, and h are the perturbation amplitudes of the grid motion about the mean positions, ξ, η, and ζ. Having defined the grid motion, the unsteady flow field is represented by the perturbation series

$$\hat{\mathbf{U}}(\xi,\eta,\zeta,\tau) = \mathbf{U}(\xi,\eta,\zeta) + \mathbf{u}(\xi,\eta,\zeta)e^{j\omega t} \quad (3)$$

Substitution of Eqs. (2) and (3) into Eq. (1) and collection of the terms that are first-order in the perturbations $\mathbf{u}$ and $(f,g,h)^T$ results in the linearized Euler equations,

$$j\omega\mathbf{u} + \frac{\partial}{\partial\xi}\left(\frac{\partial\mathbf{F}}{\partial\mathbf{U}}\mathbf{u}\right) + \frac{\partial}{\partial\eta}\left(\frac{\partial\mathbf{G}}{\partial\mathbf{U}}\mathbf{u}\right) + \frac{\partial}{\partial\zeta}\left(\frac{\partial\mathbf{H}}{\partial\mathbf{U}}\mathbf{u}\right) - \frac{\partial\mathbf{S}}{\partial\mathbf{U}}\mathbf{u} = \mathbf{b} \quad (4)$$

where $\mathbf{b}$ is a fairly complex expression which depends on the mean flow and the prescribed grid motion [see for example (Hall and Lorence, 1992)].

Numerical Modelling of the Shock Impulse

The first question we address in this paper is: What is the proper way to discretize and linearize the Euler equations in such a way that the linearized finite difference or finite volume equations properly predict the shock impulse loads that result from the unsteady shock motion. There are two obvious approaches one can take to obtain a discretization of the linearized Euler equations. One approach (Method I) is to first discretize the nonlinear Euler equations and then linearize the resulting nonlinear finite difference equations. The other approach (Method II) is to first linearize the nonlinear Euler equations then discretize the resulting linearized equations. We claim here that both approaches will produce the correct result provided that the resulting difference equations are conservative (we give a more precise definition of what conservative means in the linearized case shortly). A mathematical justification of this conjecture is given below.

Due to the complexity of the three-dimensional Euler equations, we consider the simpler one-dimensional model equation given by

$$\frac{\partial\hat{U}}{\partial t} + \frac{\partial\hat{F}}{\partial x} + B\hat{P} = 0 \quad (5)$$

where $\hat{F} = \hat{F}(\hat{U})$, $\hat{P} = \hat{P}(\hat{U})$, and $B = B(x)$. This model equation is very similar in form to the quasi-one-dimensional Euler equations which describe flow in a channel with a spatially varying cross sectional area. Since $\hat{F}$ and $\hat{P}$ are in general nonlinear functions of the conservation variable $\hat{U}$, this model equation is nonlinear.

As before, we model the conservation variable $\hat{U}$ as the sum of a mean part U plus a small harmonic perturbation $ue^{j\omega t}$. The mean solution is governed by

$$\frac{\partial F}{\partial x} + BP = 0 \quad (6)$$

where $F = F(U)$ and $P = P(U)$. The linearized unsteady model equation is given by

$$j\omega u + \frac{\partial}{\partial x}\left(\frac{\partial F}{\partial U}u\right) + B\frac{\partial P}{\partial U}u = 0 \quad (7)$$

where u is the perturbation solution, and $\partial F/\partial U$ and $\partial P/\partial U$ are steady flow Jacobians.

Returning for the moment to the unsteady nonlinear model equation, Eq. (5), it is well known that because the model equation is nonlinear, it will in general admit genuine solutions, that is, solutions with flow discontinuities. In smooth regions of the flow, the genuine solutions satisfy the differential equation, Eq. (5). The *weak* solution is that genuine solution which also satisfies the integral relation

$$\iint \left(g_t\hat{U} - g_x\hat{F}\right)dx\,dt + \int g(x,0)\,\hat{U}(x,0)\,dx = 0 \quad (8)$$

for every test function $g(x,t)$ which vanishes for large x or t and which has continuous first derivatives (Lax, 1954; Lax and Wendroff, 1960). One can then show that the unsteady Rankine-Hugoniot shock jump conditions at flow discontinuities are given by

$$\dot{X}_s\left[\!\left[\hat{U}\right]\!\right] - \left[\!\left[\hat{F}\right]\!\right] = 0 \quad (9)$$

where the symbol $[[\cdots]]$ denotes the jump in the enclosed quantity across the shock, and $\dot{X}_s$ is the velocity of the shock.

If one then considers an unsteady flow with small harmonic unsteadiness, one may linearize Eq. (9) to obtain the linearized shock jump conditions (Hall and Crawley, 1989)

$$j\omega x_s[\![U]\!] - \left[\!\left[\frac{\partial F}{\partial U}u\right]\!\right] - x_s\left[\!\left[\frac{\partial F}{\partial x}\right]\!\right] = 0 \quad (10)$$

where u is the small disturbance part of the unsteady flow and x_s is the small complex amplitude of the shock motion. Noting that the steady flow solution is given by $\partial F/\partial x = -BP$, Eq. (10) may be rewritten as

$$j\omega x_s[\![U]\!] - \left[\!\left[\frac{\partial F}{\partial U}u\right]\!\right] + x_sB[\![P]\!] = 0 \quad (11)$$

A graphical interpretation of Eq. (11) is shown in Fig. 1. Shown are the mean and unsteady flow shock trajectories as well as the resulting unsteady flow, $\hat{U}$, the mean flow U, and the perturbation flow, u. Note that u is just the difference between the unsteady and mean flows, $u = \hat{U} - U$. Further note that near the shock, an impulse in u appears due to the motion of the shock. In the limit as the unsteadiness in the flow tends toward zero, the integrated value of this impulse is given by

$$I_u = \int_{X_S-\epsilon}^{X_S+\epsilon} u\,dx = -x_s[[U]] = -x_s(U_2 - U_1) \quad (12)$$

Finally, Eq. (11) may be written as

$$j\omega I_u + \left[\!\left[\frac{\partial F}{\partial U}u\right]\!\right] + BI_p = 0 \quad (13)$$

We presently demonstrate that the weak solution of the linearized unsteady model equation, Eq. (7), produces an equivalent shock jump condition. Multiplying Eq. (7) by a test function $g(x)$ and integrating the result over the solution domain $x \in [0,L]$, we obtain

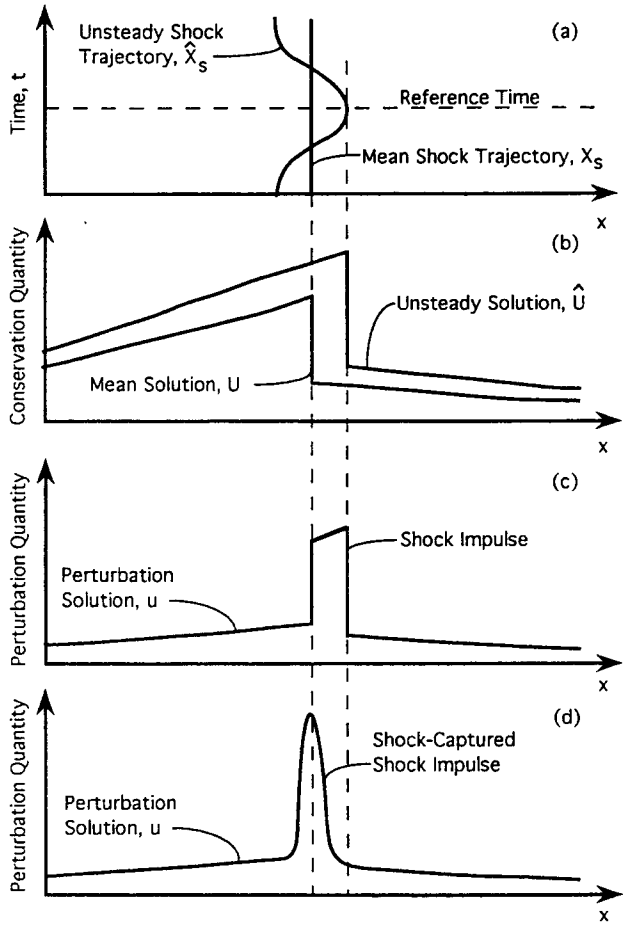

Figure 1: Top to bottom: a) Trajectory of shock in a channel or on an airfoil surface; b) Mean and unsteady flow distribution; c) Perturbation flow showing shock impulse; d) same as c) with impulse modelled by shock capturing. Note that the area under the impulse is the same as in c).

$$\int_0^L g(x)\left[j\omega u + \frac{\partial}{\partial x}\left(\frac{\partial F}{\partial U}u\right) + B\frac{\partial P}{\partial U}u\right]dx = 0 \qquad (14)$$

Integration by parts applied to the middle term in Eq. (14) gives

$$\int_0^L \left[j\omega g u - \frac{dg}{dx}\frac{\partial F}{\partial U}u + gB\frac{\partial P}{\partial U}u\right]dx + \left(g\frac{\partial F}{\partial U}u\right)\Big|_0^L = 0 \qquad (15)$$

Next we let the test function $g(x)$ be given by

$$g(x) = \begin{cases} 1 & \text{if} \quad X_s - \epsilon \le x \le X_s + \epsilon \\ 0 & \text{otherwise} \end{cases} \qquad (16)$$

where X_s is the mean shock position and ϵ is a small positive number. Differentiating Eq. (16) with respect to x gives

$$\frac{dg}{dx} = \delta[x - (X_s - \epsilon)] - \delta[x - (X_s + \epsilon)] \qquad (17)$$

where $\delta[\cdots]$ is the Dirac delta function. Substitution of Eqs. (16) and (17) into Eq. (15) gives the desired shock jump conditions of the linearized unsteady model equation,

$$j\omega \int_{X_s-\epsilon}^{X_s+\epsilon} u\,dx + \left[\!\left[\frac{\partial F}{\partial U}u\right]\!\right] + B\int_{X_s-\epsilon}^{X_s+\epsilon}\frac{\partial P}{\partial U}u\,dx = 0 \qquad (18)$$

The integrals in Eq. (18) are the areas under the impulse in u and the impulse in p, the perturbations in the conservation variable and pressure, respectively, and are denoted here by I_u and I_p (See Fig. 1).

Finally then, we may write the Rankine-Hugoniot jump condition for the linearized model equation as

$$j\omega I_u + \left[\!\left[\frac{\partial F}{\partial U}u\right]\!\right] + BI_p = 0 \qquad (19)$$

This expression is identical to Eq. (13) thus demonstrating that the weak solution to the linearized unsteady model equation is the same as the linearized weak solution of the nonlinear model equation.

We conclude, therefore, that for a finite difference scheme to properly model the linearized unsteady model equation, the finite difference scheme must be stable and consistent *and* satisfy the condition given by Eq. (15) in the limit as Δx and Δt tend toward zero. In other words, the order of linearization is immaterial; what matters is whether the resulting discretization is conservative. Note that this condition is less stringent that the condition suggested by Lindquist (1991) and Lindquist and Giles (1991a, 1991b) that the discretization be both conservative and a Method I linearization. Also note the importance of the *area* of the impulse. When capturing the shock impulse, the width and height of the impulse will depend on the amount of smoothing (or artificial viscosity) in the numerical scheme. The area under the impulse, however, should be independent of the smoothing.

Method I and Method II Linearizations

To illustrate the difference between Method I and Method II linearizations, we consider again the model equation given by Eq. (5) with the source term set to zero ($B = 0$).

Method I Linearization

Consider the discretization of the nonlinear unsteady model equation, Eq. (5), using the Lax-Wendroff scheme. The one-dimensional computational grid is assumed to have constant cell size Δx and constant time step Δt. The solution at time level $n+1$ is found by Taylor expanding the solution about time level n to obtain

$$\hat{U}_i^{n+1} = \hat{U}_i^n + \Delta t\frac{\partial \hat{U}}{\partial t}\Big|_i^n + \frac{\Delta t^2}{2}\frac{\partial^2 \hat{U}}{\partial t^2}\Big|_i^n + \mathcal{O}(\Delta t^3) \qquad (20)$$

where i denotes the ith grid node in the x-direction. The time derivatives in Eq. (20) are obtained by manipulation of the original model equation, Eq. (5). Rearranging Eq. (5) gives

$$\frac{\partial \hat{U}}{\partial t} = -\frac{\partial \hat{F}(\hat{U})}{\partial x} \qquad (21)$$

Differentiating Eq. (21) with respect to time gives

$$\frac{\partial^2 \hat{U}}{\partial t^2} = -\frac{\partial}{\partial x}\left(\frac{\partial \hat{F}}{\partial \hat{U}}\frac{\partial \hat{U}}{\partial t}\right) = \frac{\partial}{\partial x}\left(\frac{\partial \hat{F}}{\partial \hat{U}}\frac{\partial \hat{F}}{\partial x}\right) \qquad (22)$$

Next, substitution of Eqs. (21) and (22) into Eq. (20) yields

$$\hat{U}_i^{n+1} = \hat{U}_i^n - \Delta t\frac{\partial \hat{F}}{\partial x}\Big|_i^n + \frac{\Delta t^2}{2}\frac{\partial}{\partial x}\left(\frac{\partial \hat{F}}{\partial \hat{U}}\frac{\partial \hat{F}}{\partial x}\right)\Big|_i^n + \mathcal{O}(\Delta t^3) \qquad (23)$$

Finally, using centered finite difference expressions to approximate the spatial derivatives, the familiar Lax-Wendroff finite difference equation is obtained, i.e.,

$$\hat{U}_i^{n+1} = \hat{U}_i^n - \frac{\Delta t}{2\Delta x}\left[\hat{F}_{i+1}^n - \hat{F}_{i-1}^n\right]$$

$$+\frac{\Delta t^2}{2\Delta x^2}\left[\left.\frac{\partial \hat{F}}{\partial \hat{U}}\right|_{i+1/2}^n \left(\hat{F}_{i+1}^n - \hat{F}_i^n\right) - \left.\frac{\partial \hat{F}}{\partial \hat{U}}\right|_{i-1/2}^n \left(\hat{F}_i^n - \hat{F}_{i-1}^n\right)\right] \quad (24)$$

The Lax-Wendroff scheme above is second-order accurate [i.e., $\mathcal{O}(\Delta x^2, \Delta t^2)$] and is conservative (for constant Δx and Δt). A Fourier stability analysis indicates the scheme is stable for CFL numbers less than unity. Lax (1954) and Lax and Wendroff (1960) have shown that if the conservative form of the Euler equations is used, and the discretization of the Euler equations satisfies numerical conservation, and further that the scheme is consistent and stable, then the shock wave speed and strength will be correctly predicted. The Lax-Wendroff scheme above satisfies these conditions and therefore will correctly predict the unsteady shock motion.

Next, we would like to determine the behavior of Eq. (24) when the unsteadiness in the flow is small compared to the mean flow field. Since the resulting equations will be linear, we may without loss of generality assume that the flow field is composed of a nonlinear steady mean flow and a small perturbation harmonic unsteady flow so that

$$\hat{U}(x,t) = U(x) + u(x)e^{j\omega t} \quad (25)$$

where u is much smaller than U. When viewed on our computational grid, Eq. (25) becomes

$$\hat{U}_i^n = U_i + u_i e^{j\omega \Delta t n} \quad (26)$$

Substitution of Eq. (26) into Eq. (24) and collecting terms of first order in the perturbation quantity u gives the desired discrete small disturbance behavior of the nonlinear finite difference equations,

$$(1 - e^{j\omega\Delta t})u_i - \frac{\Delta t}{2\Delta x}\left[\left.\frac{\partial F}{\partial U}\right|_{i+1} u_{i+1} - \left.\frac{\partial F}{\partial U}\right|_{i-1} u_{i-1}\right]$$

$$+\frac{\Delta t^2}{2\Delta x^2}\left[\left.\frac{\partial F}{\partial U}\right|_{i+1/2}\left(\left.\frac{\partial F}{\partial U}\right|_{i+1} u_{i+1} - \left.\frac{\partial F}{\partial U}\right|_i u_i\right)\right.$$

$$\left. - \left.\frac{\partial F}{\partial U}\right|_{i-1/2}\left(\left.\frac{\partial F}{\partial U}\right|_i u_i - \left.\frac{\partial F}{\partial U}\right|_{i-1} u_{i-1}\right)\right]$$

$$+\frac{\Delta t^2}{2\Delta x^2}\left[\left.\frac{\partial^2 F}{\partial U^2}\right|_{i+1/2} u_{i+1/2}(F_{i+1} - F_i)\right.$$

$$\left. - \left.\frac{\partial^2 F}{\partial U^2}\right|_{i-1/2} u_{i-1/2}(F_i - F_{i-1})\right] = 0 \quad (27)$$

Equation (27) describes the small disturbance behavior of the nonlinear Lax-Wendroff equation. One interesting feature of Eq. (27) is the appearance of the terms involving $\partial^2 F/\partial U^2$. These terms appear because of nonlinearities in the Lax-Wendroff scheme itself rather than nonlinearities of the Euler equations.

For a one-dimensional problem, Eq. (27), along with appropriate inflow and outflow boundary conditions, could be assembled into a tridiagonal matrix equation which could then be solved quite efficiently using Gaussian elimination (the Thomas algorithm). For two- and three-dimensional problems, however, this approach would be computationally expensive and require large amounts of computer storage. For these reasons, an iterative solution technique is preferred. The following explicit relaxation procedure is proposed:

$$u_i^{n+1} = u_i^n + \delta u_i^n \quad (28)$$

where δu_i is the left-hand side of Eq. (27). As Eq. (28) is marched in time, a steady state value of u_i^n will be obtained and the solution to Eq. (27) will be recovered. This procedure is similar to the pseudo-time time-marching technique proposed by Ni and Sisto (1976) for solving the linearized Euler equations. Equation (27) can be shown to be consistent with the linearized model equation, Eq. (7), with truncation errors which are $\mathcal{O}(\Delta x^2, \Delta t^2)$. A Fourier analysis of Eq. (28) reveals that the scheme is unconditionally unstable if ω is non zero. A spectral radius stability analysis, however, that takes into account the stabilizing effect of the far-field boundary conditions shows that the scheme is stable for CFL numbers less than unity (Clark, 1992).

Method II Linearization

An alternative approach to Method I is to first linearize the nonlinear unsteady flow equations, and then discretize the resulting linear equations. To illustrate this approach, we return again to the one-dimensional model equation given by Eq. (5) and, introducing the pseudo-time assumption of Ni and Sisto (1976), assume that the unsteady flow $\hat{U}(x,t)$ is composed of a nonlinear mean flow, $U(x)$, plus a small unsteady harmonic perturbation flow, $u(x,t)e^{j\omega t}$, so that

$$\hat{U}(x,t) = U(x) + u(x,t)e^{j\omega t} \quad (29)$$

Substitution of Eq. (29) into Eq. (5) and collection of first-order terms results in the pseudo-time linearized model equation

$$\frac{\partial u}{\partial t} + j\omega u + \frac{\partial}{\partial x}\left(\frac{\partial F}{\partial U}u\right) = 0 \quad (30)$$

Note that Eq. (30) is now hyperbolic in time so that it can be marched in time. Furthermore, as time advances, u will reach a steady-state value so that the solution to Eq. (7) will be recovered.

The next step is to discretize the linearized equation using the Lax-Wendroff scheme. Manipulation of Eq. (30) gives

$$\frac{\partial u}{\partial t} = -j\omega u - \frac{\partial}{\partial x}\left(\frac{\partial F}{\partial U}u\right) \quad (31)$$

and

$$\frac{\partial^2 u}{\partial t^2} = -\omega^2 u + 2j\omega\frac{\partial}{\partial x}\left(\frac{\partial F}{\partial U}u\right) + \frac{\partial}{\partial x}\left[\frac{\partial F}{\partial U}\frac{\partial}{\partial x}\left(\frac{\partial F}{\partial U}u\right)\right] \quad (32)$$

Finally, making use of centered spatial derivatives and substitution into the Taylor expansion, Eq. (20) gives the desired Lax-Wendroff formula,

$$\delta u_i^n = -\frac{j\omega\Delta t}{4}\left[u_{i+1}^n + 2u_i^n + u_{i-1}^n\right]$$

$$-\frac{\Delta t}{2\Delta x}\left[\left.\frac{\partial \overline{F}}{\partial \overline{U}}\right|_{i+1} u_{i+1}^n - \left.\frac{\partial \overline{F}}{\partial \overline{U}}\right|_{i-1} u_{i-1}^n\right]$$

$$-\frac{\omega^2\Delta t^2}{8}\left[u_{i+1}^n + 2u_i^n + u_{i-1}^n\right]$$

$$+\frac{j\omega\Delta t}{4}\frac{\Delta t}{\Delta x}\left[\left.\frac{\partial\overline{F}}{\partial\overline{U}}\right|_{i+1} u^n_{i+1} - \left.\frac{\partial\overline{F}}{\partial\overline{U}}\right|_{i-1} u^n_{i-1}\right]$$

$$+\frac{j\omega\Delta t}{2}\frac{\Delta t}{\Delta x}\left[\left.\frac{\partial\overline{F}}{\partial\overline{U}}\right|_{i+1/2} u^n_{i+1/2} - \left.\frac{\partial\overline{F}}{\partial\overline{U}}\right|_{i-1/2} u^n_{i-1/2}\right]$$

$$+\frac{\Delta t^2}{2\Delta x^2}\left[\left.\frac{\partial\overline{F}}{\partial\overline{U}}\right|_{i+1/2}\left(\left.\frac{\partial\overline{F}}{\partial\overline{U}}\right|_{i+1} u^n_{i+1} - \left.\frac{\partial\overline{F}}{\partial\overline{U}}\right|_{i} u^n_{i}\right)\right.$$

$$\left. - \left.\frac{\partial\overline{F}}{\partial\overline{U}}\right|_{i-1/2}\left(\left.\frac{\partial\overline{F}}{\partial\overline{U}}\right|_{i} u^n_{i} - \left.\frac{\partial\overline{F}}{\partial\overline{U}}\right|_{i-1} u^n_{i-1}\right)\right] \qquad (33)$$

As in the Method I discretization [Eq. (27)], the Method II discretization [Eq. (33)] is consistent with the linearized model equation [Eq. (7)] with truncation errors which are $\mathcal{O}(\Delta x^2, \Delta t^2)$.

Note that the Method II discretization [Eq. (33)] differs significantly from that obtained using Method I [Eq. (27)]. In particular, the unsteady terms involving ω are somewhat different, and the quasi-steady terms involving $\partial^2 F/\partial U^2$ in Eq. (27) do not appear in Eq. (33). Clearly, the order in which the linearization is performed is important in determining the precise form of the difference equations.

Test for Linearized Conservation

Consider the Method I discretization of the model equation, Eq. (27). The one-dimensional computational grid has M nodes. To test for conservation, Eq. (27) is multiplied by $g_i \Delta x/\Delta t$ (where $g_i = g(x_i)$) and summed over the computational domain. After some manipulation including summation by parts, one can show that this sum is given by

$$\frac{(1-e^{j\omega t})}{\Delta t}\sum_{i=1}^{M} u_i g_i\,\Delta x + \sum_{i=2}^{M-1}\frac{g_{i+1}-g_{i-1}}{2\,\Delta x}\left.\frac{\partial F}{\partial U}\right|_i u_i\,\Delta x$$

$$- g_M \left.\frac{\partial F}{\partial U}\right|_M u_M + g_1 \left.\frac{\partial F}{\partial U}\right|_1 u_1 + \mathcal{O}(\Delta x, \Delta t) \qquad (34)$$

In the limit as $\Delta t, \Delta x \to 0$, Eq. (34) approaches Eq. (15). Therefore, this Method I linearization of the Lax-Wendroff scheme is conservative (at least for the case considered here of constant $\Delta t, \Delta x$). A similar analysis of Method II reveals that is also conservative. Hence, *both* methods should correctly predict the shock impulse.

Two- and Three-Dimensional Linearized Euler Solvers

The two- and three-dimensional linearized Euler analyses used in these codes have been previously described (Hall and Clark, 1991a; Lorence, 1991; Hall and Lorence, 1992; Clark, 1992). We therefore briefly outline the computational method used to calculate the unsteady flow field and refer the interested reader to the above references for more detail.

The general solution procedure is as follows. First, an H-grid is generated for a single blade passage of the cascade. The mean flow field is then computed using a conservative nonlinear steady Euler solver. Then, for each interblade phase angle, vibratory mode shape, and reduced frequency of interest, the unsteady grid motion is prescribed. The mean flow field and prescribed blade motion are then used to form the variable coefficients and the inhomogeneous part of the linearized Euler equations. Finally, the linearized Euler equations are solved in a single computational passage using the pseudo-time technique proposed by Ni and Sisto (1976). Ni's Lax-Wendroff scheme (Ni, 1982; Dannenhoffer, 1987; Ni and Bogoian, 1989) is used to discretize and solve the pseudo-time linearized Euler equations. For the comparisons presented in this paper, we have developed both Method I and Method II versions of the linearized unsteady Euler solver. Both Method I and Method II schemes are second-order accurate $[\mathcal{O}(\Delta x^2, \Delta t^2)]$. A combination of second and fourth difference smoothing is used to eliminate sawtooth modes and capture shocks. Ni's multiple grid acceleration technique is used to speed convergence.

In the present analysis, we assume that the blade row is an isolated blade row in an infinitely long duct. The computational domain, however, is finite in extent. At the far-field computational boundaries, nonreflecting boundary conditions are applied to prevent spurious reflections of outgoing pressure, entropy, and vorticity waves back into the computational domain (Hall, Lorence, and Clark, 1993).

For transonic flow calculations, a conservative discretization is required to model accurately the shock impulse. For Ni's two-dimensional scheme to be conservative, the ratio of the cell time step to the cell area must be a constant throughout the computational domain (in the three-dimensional scheme, the ratio of the time step to the cell volume must be constant). Furthermore, for stability, the CFL restriction must not be violated anywhere in the domain. This means that the time step used in some computational cells may be much smaller than the maximum permissible time step for that cell, greatly slowing the convergence of the scheme, even when using multiple grid acceleration. To overcome this difficulty, we propose the following modification to the linearized scheme. Consider again the finite difference representation of the linearized model problem [Eq. (27)]. We modify this equation such that

$$u_i^{n+1} = u_i^n + R_i\,\delta u_i^n \qquad (35)$$

where δu_i^n is as before and R_i is an over-relaxation factor. In the present analysis we have taken this factor to be roughly equal to the maximum permissible local time step size divided by the actual conservative time step.

A Fourier analysis shows that for over-relaxation factors greater than unity, Eq. (35) produces an unconditionally unstable scheme. It would seem, therefore, that over-relaxation would not be useful. However, for transonic flow calculations, smoothing must be added to the scheme to capture shocks. This smoothing stabilizes the over-relaxation scheme so long as the over-relaxation factor is not too large. Hence, a clamp is also applied so that the maximum over-relaxation factor can be no larger than about five. As we will demonstrate, the over-relaxation scheme is stable and significantly reduces the computational time required to obtain a converged solution.

RESULTS

Transonic Channel Flow

To test the present linearized Euler analyses, we first consider the transonic flow through a diverging channel. This case is presented to demonstrate the ability of the linearized Euler method to model shock motion accurately using shock capturing. We will demonstrate that both Method I and Method II linearizations will produce satisfactory results as long as they are conservative.

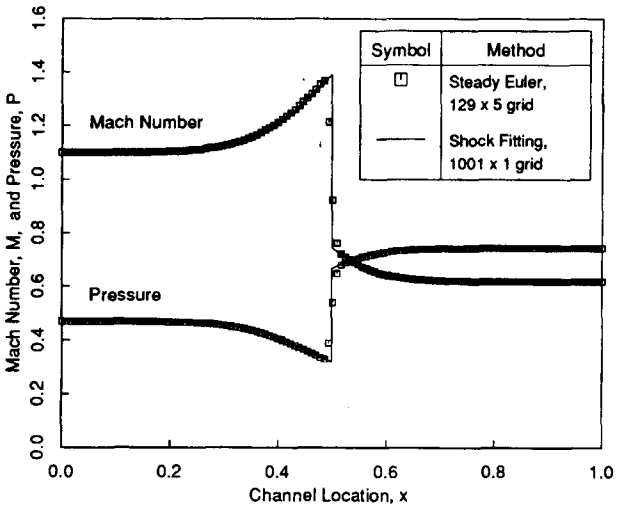

Figure 2: Steady transonic flow in a diverging channel.

The channel considered here has a height, A, given by,

$$A(x) = A_{\text{inlet}} \left\{ 1.10313 + 0.10313 \tanh \left[10 \left(x - \frac{1}{2} \right) \right] \right\}, 0 \leq x \leq 1 \tag{36}$$

(The units may be taken to be any consistent set of units.) So that we may compare the results obtained by the present method to those obtained by a one-dimensional shock-fitting theory, A_{inlet} is taken to be small compared with the channel length ($A_{\text{inlet}} = 0.01$). The inflow total pressure, P_T, total density, ρ_T, and flow velocity, U, are 1.0, 1.364, and 1.0 respectively. The back pressure, P_{exit}, is 0.7422. Shown in Fig. 2 is the Mach number and pressure distribution as computed using the present nonlinear steady Euler solver on a 129 × 5 node computational grid. The grid was generated so that the computational cells all have the same area, ΔA. The time step, Δt, used in these calculations was constant throughout the computational domain unless otherwise noted. Constant Δt and ΔA were chosen because Ni's scheme is only conservative if the ratio $\Delta t / \Delta A$ is constant throughout the computational domain.

Also shown for comparison in Fig. 2 is the solution determined using a steady quasi-one-dimensional, shock-fitting Euler solver using 1001 grid nodes in the x-direction. The shock-fitting Euler solution is grid converged and may be taken to be the exact solution. Note the excellent agreement between the two different approaches. The only noticeable differences occur at the shock, where the present nonlinear Euler analysis smears the shock over about five grid nodes.

Next, we consider a quasi-steady perturbation in the back pressure. The perturbation solution was calculated using four different approaches. First, the solution was calculated using a quasi-one-dimensional, shock-fitting, linearized Euler analysis. This solution was computed on an extremely fine grid (1001 nodes in the x-direction) and is essentially the exact solution. Next, the present nonlinear steady Euler solver was used to compute two nonlinear solutions at slightly different back pressures. These two solutions were then subtracted one from the other and the result was normalized by the difference in back pressures to obtain the perturbation solution. Finally, the solution was determined using the present linearized Euler analysis (both Methods I and II). It should be noted that for this comparison the usual nonreflecting

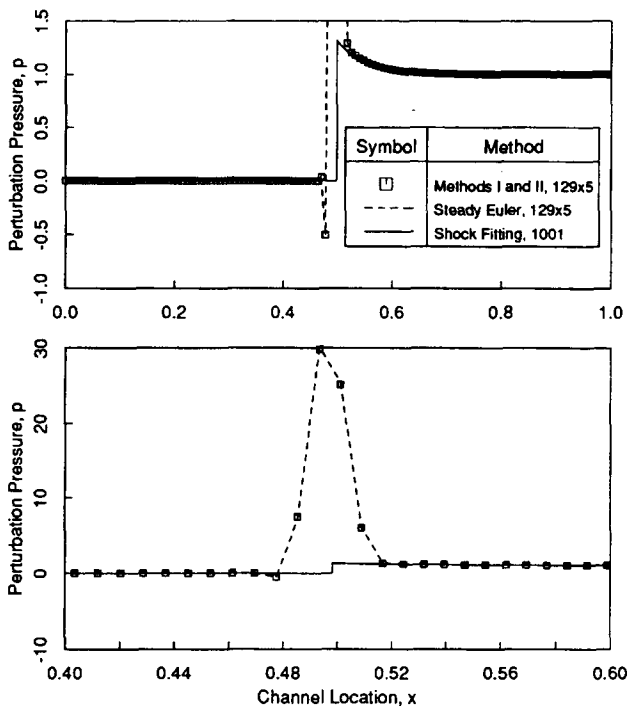

Figure 3: Top: Perturbation pressure in a diverging channel due to a steady perturbation in back pressure. Bottom: Enlarged view of the shock impulse region.

far-field boundary conditions were replaced with reflecting boundary conditions. Upstream the perturbation in total pressure and density as well as the inflow angle was set to zero. Downstream the perturbation in static pressure was prescribed. These boundary conditions for this model problem were chosen for their simplicity and are not meant to model any real physical system. The results of these various approaches are shown in Fig. 3. The Method I and Method II results are indistinguishable from one another and are therefore plotted with a single symbol. As expected, all of the solutions are in excellent agreement in regions away from the shock. At the shock, however, the methods using shock-capturing produce an impulse of pressure. The area under the impulse is equal to the product of the shock displacement and the mean pressure jump across the shock. The shock impulse then represents the load exerted on the wall due to the motion of the shock. Also shown in Fig. 3 is an enlarged view of the shock region. Note that the computed results from the Method I and Method II linearizations are virtually identical to the perturbation of the nonlinear Euler analysis.

To further validate the linearized shock capturing technique for unsteady flows, we computed the unsteady pressure distribution due to an unsteady perturbation in back pressure with an excitation frequency, ω, of 1.0. The results are shown in Fig. 4. Also shown are the results of a quasi-one-dimensional, unsteady, shock-fitting, linearized Euler solver. Away from the shock, the results agree quite well with the Method I and II results. At the shock, the present Method I and II solutions show an impulse. This impulse represents the unsteady load acting on the channel wall due to the motion of the shock.

To determine whether the present linearized Euler solver correctly predicts the unsteady loads induced by the shock motion,

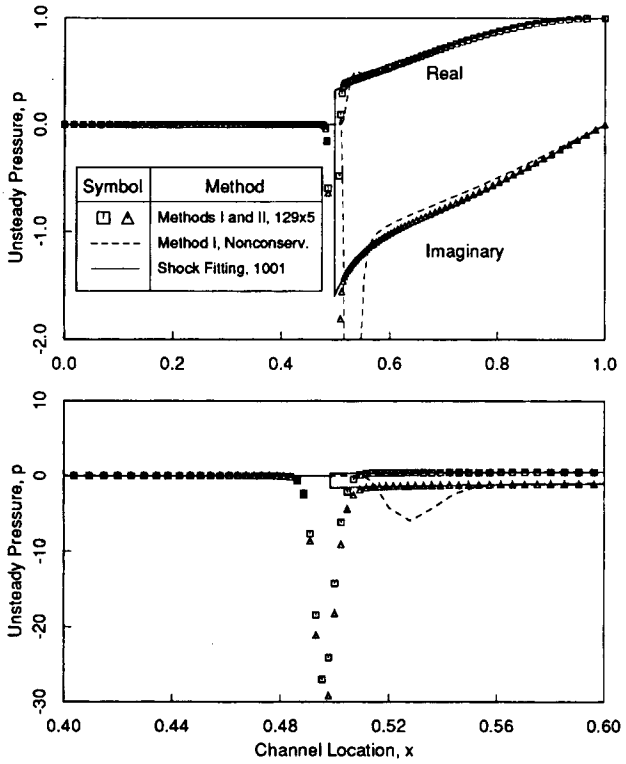

Figure 4: Top: Unsteady pressure in a diverging channel due to an unsteady perturbation in back pressure, $\omega = 1.0$. Bottom: Enlarged view of the shock impulse region.

the pressure was integrated over the lower channel wall to determine the net wall force. The results from this analysis are tabulated in Table 1 for several different frequencies. Also tabulated in Table 1 is the wall force computed using the linearized unsteady shock-fitting code. The agreement between the conservative form of the Method I and Method II analyses are seen to be in almost perfect agreement with the shock fitting scheme for all frequencies suggesting that the shock impulse found using shock capturing is properly modelled. Even in the higher frequency cases the agreement is quite good, although there is a slight error (about 0.5°) in the phase of the wall force. We believe that these differences arise from the dispersion errors in the solution away from the shock rather than from a limitation in shock capturing at high reduced frequencies.

Finally, for the $\omega = 1.0$ case, we deliberately made the Method I and II calculations nonconservative to demonstrate that the shock impulse cannot be properly modelled using a nonconservative algorithm. In the Method I calculation, the time step Δt was held constant throughout the domain, but a grid with variable cell areas near the shock was used. In the Method II calculations, the cell areas ΔA were constant throughout the computational domain, but the time step used in each computational cell was based on a local CFL number (local time stepping). In both cases, the ratio $\Delta t/\Delta A$ varies over the computational domain making the schemes nonconservative. As shown in Table 1, the incorrect wall force is predicted whenever the scheme is nonconservative. In the Method I case (see also Fig. 4), the phase of the wall force is in error by about 32.1°. The phase error in the Method II example is 6.2°.

Table 1: Predicted pressure loads in a transonic diverging channel due to an unsteady perturbation in back pressure using a uniform area computational grid.

Frequency	Scheme	Wall Force	
0.0	1D Shock Fitting	$1.0305 \angle\ 0.0°$	
	Nonlinear Euler[a]	$1.0346 \angle\ 0.0°$	
	Method I	$1.0273 \angle\ 0.0°$	
	Method II	$1.0273 \angle\ 0.0°$	
1.0	1D Shock Fitting	$0.6390 \angle\ -78.7°$	
	Method I	$0.6353 \angle\ -78.8°$	
	Method II	$0.6354 \angle\ -78.8°$	
	Method I	$0.5397 \angle\ -46.6°$	Nonconservative [b]
	Method II	$0.6229 \angle\ -84.9°$	Nonconservative [c]
2.0	1D Shock Fitting	$0.1974 \angle\ -114.1°$	
	Method I	$0.1983 \angle\ -113.6°$	
	Method II	$0.1984 \angle\ -113.6°$	

[a]Results from the steady analysis were found for two slightly different back pressures. The two solutions were then differenced and normalized by ΔP_{exit}.
[b]Time accurate time marching steady and unsteady solution on a nonuniform area computational grid.
[c]Local time stepping used in steady and unsteady analyses.

From these numerical results we conclude that both Method I and Method II linearizations will produce satisfactory results if and only if the linearizations are conservative. However, since the Method I linearization is predicated on the assumption that a constant time step is used throughout the computational domain, this precludes the use of Method I for most problems since it would be difficult and undesirable to generate computational grids with constant cell areas throughout the computational domain. With the Method II analysis, we only require that $\Delta t/\Delta A$ be constant for the scheme to be conservative. Therefore, for the remaining examples, we will use a conservative Method II analysis.

Unsteady Compressor and Fan Flows

Having demonstrated the ability of the present method to model transonic channel flow, we next consider the unsteady flow in compressors and fans.

Tenth Standard Configuration

The first cascade considered is the Tenth Standard Configuration (Bölcs and Fransson, 1986; Fransson, 1991). The airfoils of this cascade have a NACA 0006 thickness distribution slightly modified so that the trailing edge is wedged rather than blunt. The camber line is a circular arc with a maximum height of 5 percent of the chord. The flow conditions are such that there is a supersonic patch on the suction surface of the airfoil. The stagger angle, Θ, is 45° and the gap-to-chord ratio, G, is 1.0. The mean inflow angle, $\beta_{-\infty}$, is 58° and the inflow Mach number, $M_{-\infty}$, is 0.8. Figure 5 shows the computed coefficient of pressure distribution along the airfoil surface calculated using the present nonlinear steady Euler code. The grid used for this calculation was a 193×49 node H-grid with a total of 193 nodes on the airfoil surface. Note in particular the transonic patch on the suction surface of the airfoil. The present steady Euler solver captures the

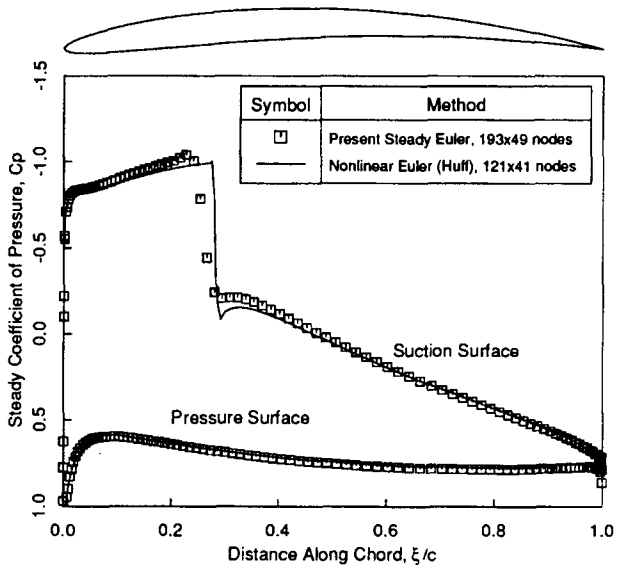

Figure 5: Coefficient of pressure distribution, Tenth Standard Configuration: $M_{-\infty} = 0.8, G = 1.0, \Theta = 45°, \Omega_{-\infty} = 58°$

shock over about five grid points. Also shown is the a nonlinear Euler solution provided by Huff based on a flux difference splitting algorithm (1989, 1992).

With the steady solution now known, consider the case where the airfoils plunge with an interblade phase angle, σ, of $-90°$ and a reduced frequency, $\bar{\omega}$ (based on the upstream velocity and blade chord), of 1.287. Figure 6 shows the computed unsteady pressure distribution on the airfoil surface using Method II linearization. The impulsive shock load is clearly visible on the suction surface. Also shown for comparison is the pressure distribution computed using Huff's nonlinear time-marching algorithm. The agreement between the present linearized analysis and the nonlinear time-marching Euler analysis is excellent away from the shock. Shown in the table insert in Fig. 6 is the magnitude and phase of the resulting unsteady lift. The magnitude of the unsteady lift calculated using the two different approaches agrees within about 2%; the phase differs by only about 3°. Note that the shock impulse predicted by the present unsteady linearized Euler analysis is somewhat narrower and taller than that predicted by the nonlinear code. The *areas* of the impulses, however, are very nearly equal. Furthermore, the unsteady load due to the impulse is of the same order of magnitude as the unsteady load due to the unsteady pressure distribution away from the shock.

Because conservative Method II linearizations require that the ratio $\Delta t/\Delta A$ be constant throughout the computational domain, the time step taken in a particular computational cell may be considerably smaller than the maximum permitted for stable calculations. The result is that the convergence will be considerably slower than if the local maximum permissible time step had been taken everywhere (local time stepping). To overcome this problem, we use conservative time stepping in conjunction with multiple grid acceleration and over-relaxation. Figure 7 shows the convergence histories for three linearized unsteady flow calculations for the previous example: one using local time stepping with multigrid, one using conservative time stepping with multigrid, and one using conservative time stepping with over-relaxation plus multigrid.

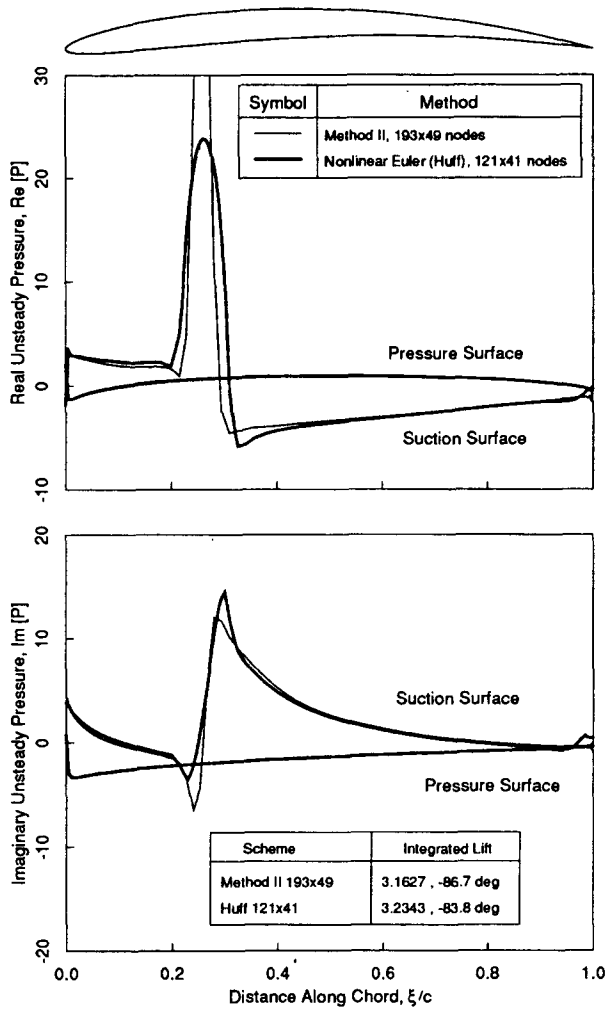

Figure 6: Real and imaginary unsteady surface pressure, Tenth Standard Configuration, plunging: $\omega = 1.287, \sigma = -90°$

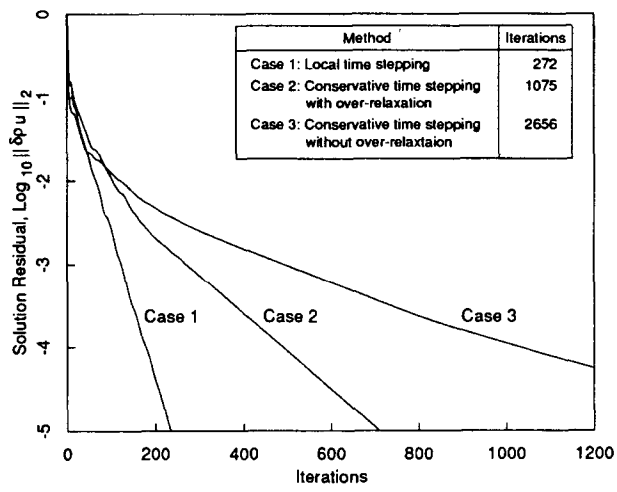

Figure 7: Convergence histories of unsteady solution for different methods. All cases use multigrid acceleration.

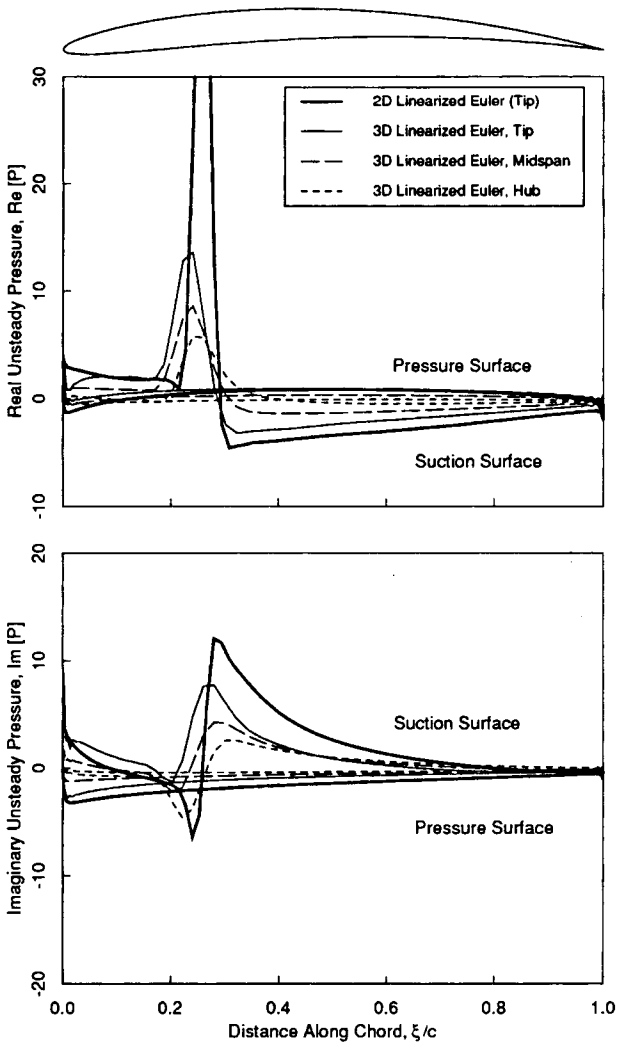

Figure 8: Real and imaginary unsteady surface pressure, Tenth Standard Configuration, plunging, airfoils vibrating in first bending mode: $\omega = 1.287, \sigma = -90°$

Note that over-relaxation reduces the computational time required by a factor of about 2.5 compared to conservative time stepping without over-relaxation. Finally, we should mention that a comparable nonlinear time marching algorithm would require about 20 to 50 times the computational time required by the global time step calculations with over-relaxation and multigrid.

Next, we consider a three-dimensional linear cascade of Tenth Standard Configuration airfoils. The airfoils have an aspect ratio of 2. The steady flow conditions are the same as in the two-dimensional problem. The solution was computed on a $129 \times 33 \times 17$ node H-grid. For the unsteady flow problem, the airfoils are again assumed to vibrate in plunge with an interblade phase angle, σ, of $-90°$ and a reduced frequency, $\overline{\omega}$, of 1.287. The mode shape is assumed to be the first bending mode shape of a cantilevered beam. Figure 8 shows the real and imaginary parts of the unsteady pressure distribution at three spanwise stations. Also shown is the two-dimensional "strip theory" result at the tip. Shown in Figure 9 are contours of unsteady pressure on the pressure and suction surfaces. Note the shock impulse on the suction surface.

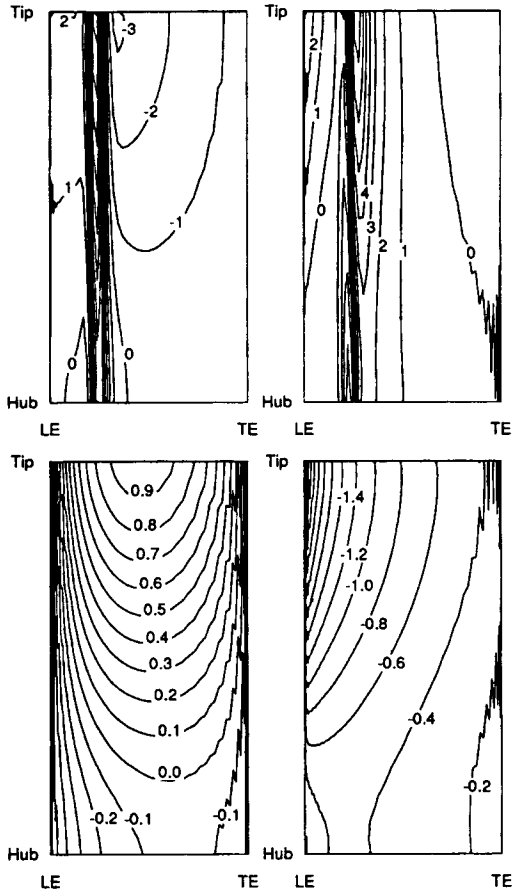

Figure 9: Unsteady surface pressure contours, Tenth Standard Configuration, plunging, airfoils vibrating in first bending mode: $\omega = 1.287, \sigma = -90°$ Top: real (left) and imaginary (right) parts of unsteady pressure on suction surface. Bottom: real (left) and imaginary (right) parts of unsteady pressure on pressure surface.

For comparison, the contours predicted by two-dimensional strip theory are shown in Fig. 10. These results clearly indicate the need to model three-dimensional effects. For example, the unsteady pressures at the tip of the blade are significantly less than would be predicted by strip theory. Furthermore, the unsteady load at the hub is not zero as would be predicted by strip theory.

High Speed Cascade

The next case considered is a two-dimensional cascade of fan blades with a relative inlet Mach number, $M_{-\infty}$, of 1.2, stagger angle, Θ, of 55°, and blade-to-blade gap, G, of 1.0. This case is presented to demonstrate the importance of moving shocks on the aeroelastic response of fan blades. Figure 11 shows the steady pressure contours. The solution was computed on a 129×33 node grid with a total of 129 nodes on the airfoil surface. Figure 12 shows the computed isentropic Mach number on the airfoil's surface. The pressure rise due to the passage shock can be clearly seen on both the suction and pressure surfaces. The shock is smeared over about four grid nodes.

Next, we computed the unsteady aerodynamic response of the cascade for a range of interblade phase angles. The airfoils

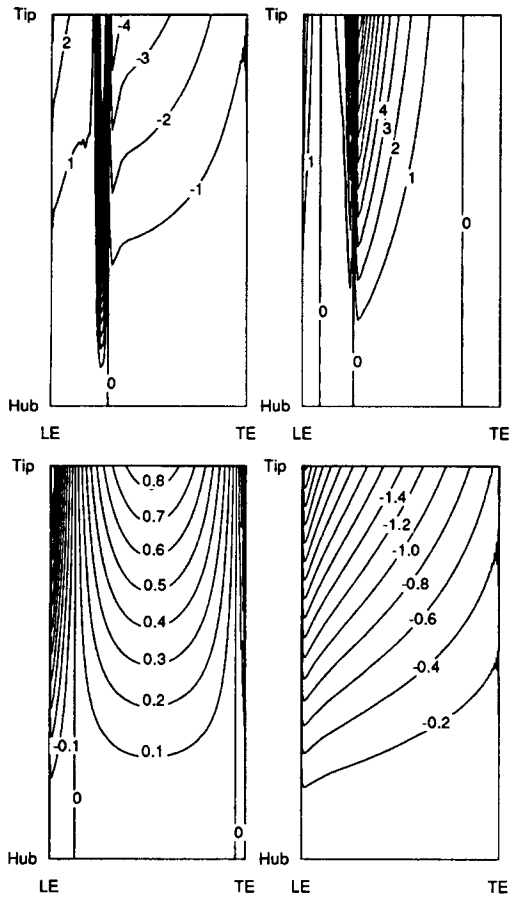

Figure 10: Unsteady surface pressure contours, Tenth Standard Configuration, plunging, airfoils vibrating in first bending mode, two-dimensional strip theory approximation: $\omega = 1.287, \sigma = -90°$ Top: real (left) and imaginary (right) parts of unsteady pressure on suction surface. Bottom: real (left) and imaginary (right) parts of unsteady pressure on pressure surface.

pitch about their midchords with a reduced frequency, $\overline{\omega}$, of 0.5. For each interblade phase angle, the computed unsteady surface pressure was integrated to obtain the unsteady pitching moment. Shown in Fig 13 is the imaginary part of the unsteady pitching moment as a function of interblade phase angle. Positive imaginary pitching moments correspond to negative aerodynamic damping which will produce flutter for tuned cascades. Note that for $\sigma = 120°$, the cascade is slightly unstable.

Shown in Fig. 14 is the unsteady pressure for the case where the airfoils vibrate in pitch with a reduced frequency, $\overline{\omega}$, of 0.5 and interblade phase angle, σ, of 120°. Note that the unsteady aerodynamic load on the airfoil is dominated by the shock impulses. The impulse acting near the trailing edge provides a positive contribution to the imaginary part and hence is destabilizing. The impulse near the leading edge, on the other hand, is stabilizing. While these results demonstrate the importance of unsteady shock motion on the unsteady aerodynamic behavior of the fan, it should be noted that whenever strong in-passage shocks occur, viscous effects become important due to the large adverse pressure gradient at the shock. These effects are not modelled here.

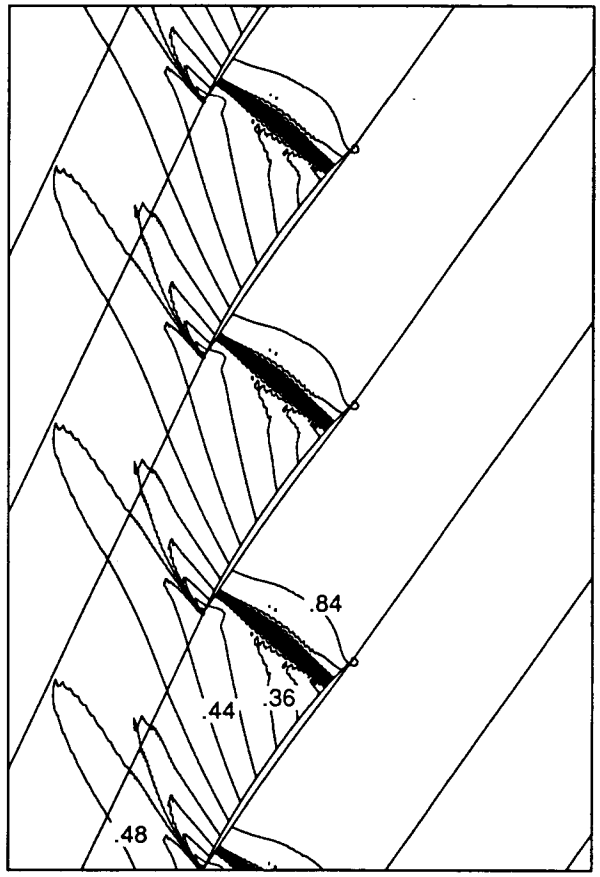

Figure 11: Steady pressure contours, modified circular arc airfoil: $M_{-\infty} = 1.2, G = 1.0, \Theta = 55°, \Omega_{-\infty} = 60°$

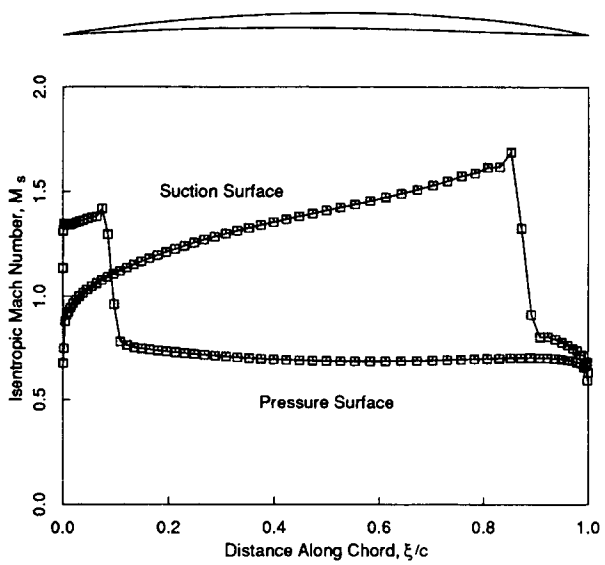

Figure 12: Isentropic Mach number distribution, modified circular arc airfoil: $M_{-\infty} = 1.2, G = 1.0, \Theta = 55°, \Omega_{-\infty} = 60°$

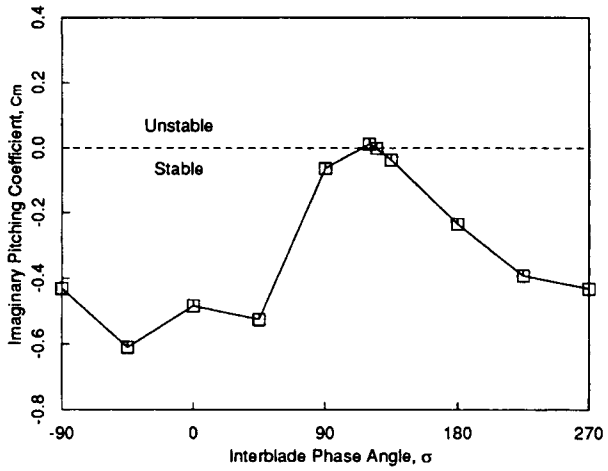

Figure 13: Imaginary part of moment coefficient for a range of interblade phase angles, modified circular arc airfoil, pitching about midchord, $\omega = 0.5$.

CONCLUDING REMARKS

In this paper, we have presented a linearized Euler analysis of two- and three-dimensional unsteady transonic flows in channels and cascades. Two different types of linearization were examined. Using Method I, the nonlinear Euler equations are first discretized using a conservative, time-accurate Lax-Wendroff scheme. The resulting nonlinear finite volume discretization is then linearized. Using Method II, the Euler equations are first linearized and then discretized using a Lax-Wendroff scheme. It was shown mathematically and by numerical experiment that the both Method I and Method II linearizations correctly predict the unsteady shock impulse in transonic flows if and only if the scheme is conservative; the order of linearization and discretization appears to be inconsequential. When either the Method I or Method II discretizations were made nonconservative by using a non-constant $\Delta t/\Delta A$, the shock impulse was found to be incorrectly predicted even though the methods are formally second-order accurate and consistent with the linearized Euler equations.

Because a constant $\Delta t/\Delta A$ is required in the steady and unsteady flow calculations to insure conservation, the time step taken at a computational cell may be significantly smaller than the maximum local permissible time step for stability. This small time step in turn slows convergence of the scheme. To overcome this difficulty, an over-relaxation technique was proposed that dramatically improves the convergence rate of the linearized Euler analysis while leaving the method fully conservative. When coupled with Ni's multiple grid acceleration technique, the present linearized Euler solver can compute unsteady transonic flows nearly two orders-of-magnitude faster than a comparable nonlinear time-accurate time-marching solver.

A number of two- and three-dimensional unsteady transonic flows in cascades were computed using the linearized Euler analyses. Where possible, these results were compared to a nonlinear time-accurate time-marching scheme and found to be in excellent agreement. Furthermore, the unsteady shock load was found to be a significant contributor to the unsteady aerodynamic forces acting on the airfoil.

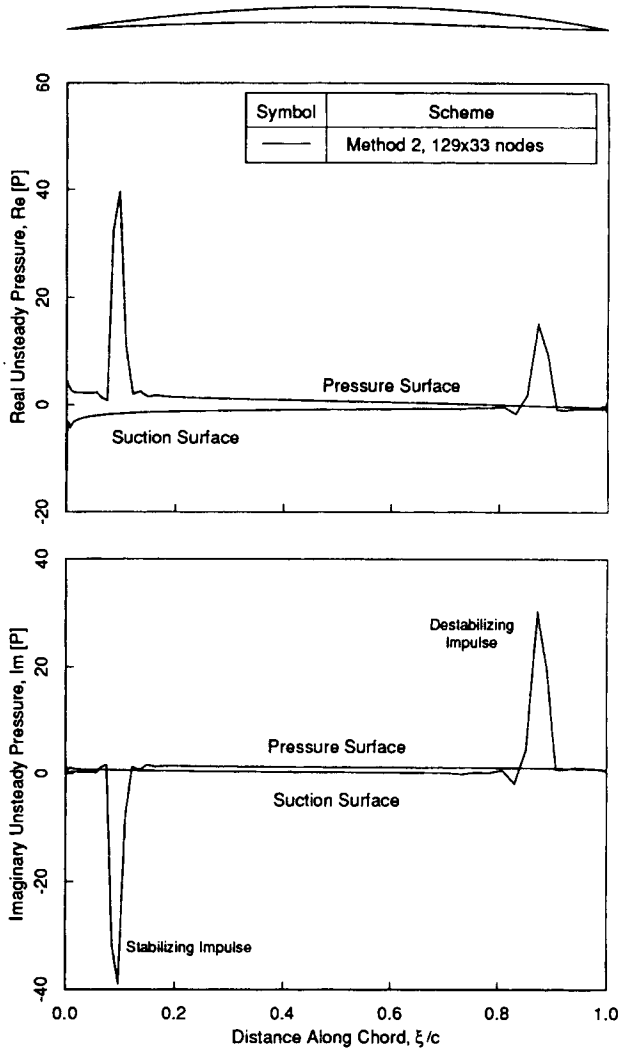

Figure 14: Real and imaginary unsteady surface pressure, modified circular arc airfoil, pitching about midchord: $\omega = 0.5, \sigma = 120°$

ACKNOWLEDGMENTS

This work was supported by NASA Grant NAG3-1192 with Dr. Daniel Hoyniak serving as technical monitor, and by a research contract from General Electric Aircraft Engines with Dr. Andrew Chuang serving as technical monitor. Additional support was provided by the National Science Foundation through a Presidential Young Investigator award to the first author. The authors wish to thank Dr. Dennis Huff of NASA Lewis Research Center for providing computational results which are presented in this paper. The authors also wish to acknowledge helpful discussions on the topic of shock capturing with Dr. Dana Lindquist and Dr. Michael Giles while they were at M.I.T., and Dr. Graham Holmes of the General Electric Company Research and Development Center.

REFERENCES

Bölcs, A., and Fransson, T. H., 1986, Aeroelasticity in Turbomachines Comparison of Theoretical and Experimental Cascade

Results, Air Force Office of Scientific Research, AFOSR-TR-87-0605.

Clark, W. S., 1992, "Prediction of Unsteady Flows in Turbomachinery Using the Linearized Euler Equations on Deforming Grids," M. S. Thesis, Duke University.

Dannenhoffer III, J. F., 1987, "Grid Adaptation for Complex Two-Dimensional Transonic Flows," Sc. D. Thesis, Massachusetts Institute of Technology.

Fransson, T. H., 1991, Private communication.

Hall, K. C., and Crawley, E. F., 1989, "Calculation of Unsteady Flows in Turbomachinery Using the Linearized Euler Equations," *AIAA Journal*, Vol. 27, No. 6, pp. 777-787.

Hall, K. C. and Clark, W. S., 1991a, "Prediction of Unsteady Aerodynamic Loads in Cascades Using the Linearized Euler Equations on Deforming Grids," Presented at the AIAA/SAE/ASME/-ASEE 27th Joint Propulsion Conference. AIAA Paper 91-3378.

Hall, K. C. and Clark, W. S., 1991b, "Calculation of Unsteady Linearized Euler Flows in Cascades Using Harmonically Deforming Grids," Presented at the Sixth Symposium on Unsteady Aerodynamics and Aeroelasticity of Turbomachines and Propellers, Notre Dame, IN.

Hall, K. C. and Lorence, C. B., 1992, "Calculation of Three-Dimensional Unsteady Flows in Turbomachinery Using the Linearized Harmonic Euler Equations," Presented at the International Gas Turbine and Aeroengine Congress and Exposition, Cologne, Germany, June 1-4. ASME Paper 92-GT-136.

Hall, K. C., Lorence, C. B., and Clark, W. S., 1993, "Nonreflecting Boundary Conditions for Linearized Aerodynamic Calculations," Presented at the AIAA 31st Aerospace Sciences Meeting, Reno, NV. AIAA Paper 93-0882.

Holmes, D. G. and Chuang, H. A., 1991, "2D Linearized Harmonic Euler Flow Analysis for Flutter and Forced Response," Presented at the Sixth Symposium on Unsteady Aerodynamics and Aeroelasticity of Turbomachines and Propellers, Notre Dame, IN.

Huff, D. L. and Reddy, T.S.R., 1989, "Numerical Analysis of Supersonic Flow Through Oscillating Cascade Sections by Using a Deforming Grid." AIAA Paper 89-2805.

Huff, D. L., 1992, Private communication.

Kahl, G. and Klose, A., 1991, "Time Linearized Euler Calculations for Unsteady Quasi-3D Cascade Flows," Presented at the Sixth Symposium on Unsteady Aerodynamics and Aeroelasticity of Turbomachines and Propellers, Notre Dame, IN.

Lax, P. D., 1954, "Weak Solutions of Nonlinear Hyperbolic Equations and Their Numerical Computation," *Comm. Pure Appl. Math*, Vol. 7, pp. 159-193.

Lax, P. D. and Wendroff, B., 1960, "Systems of Conservation Laws," *Comm. Pure Appl. Math*, Vol. 13, pp. 217-237.

Lindquist, D. R., 1991, "Computation of Unsteady Transonic Flowfields Using Shock Capturing and the Linear Perturbation Euler Equations," Ph. D Thesis, Massachusetts Institute of Technology.

Lindquist, D. R. and Giles, M. B., 1991a,"On the Validity of Linearized Unsteady Euler Equations With Shock Capturing," Presented at the AIAA 10th Computational Fluid Dynamics Conference, Honolulu, HI. AIAA Paper 91-1598-CP.

Lindquist, D. R. and Giles, M. B., 1991b, Private communication.

Lorence, C. B., 1991, "An Investigation of Three-Dimensional Unsteady Flows in Turbomachinery Using the Linearized Euler Equations," M. S. Thesis, Duke University.

Ni, R. H., and Sisto, F., 1976, "Numerical Computation of Nonstationary Aerodynamics of Flat Plate Cascades in Compressible Flow," *Transactions of the ASME: Journal of Engineering for Power* , Vol. 98, pp. 165-170.

Ni, R. H., 1982, "A Multiple-Grid Scheme for Solving the Euler Equations," *AIAA Journal*, Vol. 28, No. 12, pp. 2050-2058.

Ni, R. H. and Bogoian, J. C., 1989, "Prediction of Three-Dimensional Multi-Stage Turbine Flow Field Using a Multiple-Grid Euler Solver," AIAA Paper 89-0203.

Verdon, J. M., and Caspar, J. R., 1984, "A Linearized Unsteady Aerodynamic Analysis for Transonic Cascades," *Journal of Fluid Mechanics*, Vol. 149, pp. 403-429.

Verdon, J. M., 1987, "Linearized Unsteady Aerodynamic Theory," Chapter 1 in AGARD Manual on Aeroelasticity in Axial-Flow Turbomachines, Unsteady Turbomachinery Aerodynamics, Vol. 1, M. F. Platzer and F. O. Carta (eds.), AGARD-AG-298.

Whitehead, D. S., 1987, "Classical Two-Dimensional Methods," Chapter 2 in AGARD Manual on Aeroelasticity in Axial-Flow Turbomachines, Unsteady Turbomachinery Aerodynamics, Vol. 1, M. F. Platzer and F. O. Carta (eds.), AGARD-AG-298.

Whitehead, D. S., 1990, "A Finite Element Solution of Unsteady Two-Dimensional Flow in Cascades," *International Journal For Numerical Methods in Fluids*, Vol. 10, pp. 13-34.